AIAA SciTech Forum
January 3-7, 2022, San Diego, CA & Virtual
AIAA SCITECH 2022 Forum

10.2514/6.2022-0829

Extracting Atmospheric Optical Turbulence Parameters from AAOL-BC Wavefront Measurements

Matthew Kalensky*, Eric J. Jumper †, and Stanislav Gordeyev ‡
University of Notre Dame, Notre Dame, IN, 46556

Wavefront measurements were collected from a laser beam which propagated between two aircraft at varying altitudes and separations. Various data processing procedures were employed for decoupling distortions imposed by the atmosphere and distortions imposed by the aero-optical environment in proximity of the aircraft. Atmospheric optical turbulence parameters such as C_n^2 and r_0 were then estimated from the data using different approaches. These results are compared with models prevalent in literature as well as previous experimental measurements. The atmospheric optical turbulence parameters measured in this work showed good agreement with the previous experimental measurements.

I. Nomenclature

A	=	near ground optical turbulence conditions
α	=	geometric constant for slope discrepancy
c_f	=	skin friction coefficient
C_n^2	=	index of refraction structure constant
$C_{\mathcal{T}}^2$	=	temperature structure constant
D	=	aperture diameter
d	=	lenslet diameter
δ	=	slope discrepancy
δ_{BL}	=	boundary layer thickness
E_η^2	=	atmospheric fitting error structure function
$E_\gamma^2(\tau)$	=	aero-optical/aero-acoustical fitting error structure function
E_{SD}^2	=	slope discrepancy structure function
η	=	fitting error
k	=	laser wavenumber
K_{GD}	=	Gladstone-Dale constant
λ	=	laser wavelength
M	=	Mach number
μ	=	measurement noise
n	=	index of refraction
OPD	=	optical path difference
OPL	=	optical path length
P	=	pressure
R	=	gas constant
ρ	=	density
ρ_∞	=	freestream density
r_0	=	atmospheric coherence length
σ_μ^2	=	noise variance
σ_ϕ^2	=	phase variance
T	=	large time delays
$\mathcal{T}$	=	temperature

*Graduate Researcher, Department of Aerospace and Mechanical Engineering, AIAA Student Member
†Professor, Department of Aerospace and Mechanical Engineering, AIAA Fellow
‡Associate Professor, Department of Aerospace and Mechanical Engineering, AIAA Associate Fellow

τ = time delay
U_c = wind speed
Z = propagation distance
z = propagation position

II. Introduction

In recent years, there has been interest in developing aircraft mounted high energy laser systems (HELs). Employing a laser propagation system on an aircraft has additional challenges compared to ground based optical systems. In and around the aircraft, the outgoing laser beam is subjected to distortions from aerodynamic turbulence, mechanical contamination, as well as acoustic contamination from the aircraft jet engine. The aerodynamic turbulence around the aircraft introduces distortions onto the beam due to compressibility effects and unsteady pressure fluctuations. This environment, hereafter referred to as the aero-optical environment, results in less energy on-target in the far-field. Aero-optical turbulence structures which are sufficiently smaller than the aperture, referred to as higher-order distortions, tend to energy spread in the far-field. Structures larger than, or on the order of the size of the aperture result in bulk angular motion, or tip/tilt, imposed onto the laser beam. As a consequence, this leads to pointing issues or beam jitter in the far-field. Mechanical vibrations from the aircraft also impose tip/tilt onto the laser beam. The acoustical environment around the aircraft imposes both higher-order distortions as well as tip/tilt onto the beam. These three types of distortions all originate in or around the aircraft. As the laser beam leaves the aircraft, the beam propagates through the atmosphere to a target. As has been studied for centuries, the atmospheric turbulence introduces additional aberrations onto the laser beam. Instead of compressibility effects, pressure fluctuations, or mechanical vibrations, the distortions imposed onto the laser beam from the atmosphere are primarily from temperature fluctuations carried by turbulence structures of a vast range of spatial sizes.

In this work, wavefront measurements were collected using a Shack-Hartmann wavefront sensor (SHWFS). These measurements were used to quantify the distortions imposed by the atmosphere onto a laser beam which was also subjected to aberrations from the aero-optical, mechanical, and aero-acoustical environments. In order to make these measurements, a laser beam is projected through the atmosphere at both varying altitudes as well as propagation distances using the Airborne Aero-Optics Laboratory (AAOL). AAOL is an in-flight experimental test-bed where aero-optics experiments can be performed under real conditions [1, 2]. AAOL consists of two Falcon-10 aircraft capable of flying at varying separations, altitudes, and Mach numbers. One aircraft, designated as the source aircraft, projects a 532 nm diverging laser beam onto an optical quality window mounted on the second aircraft, referred to here as the laboratory aircraft. For this experiment, the two AAOL aircraft fly at large separations to measure the distortions imposed by the atmosphere onto the laser beam. Various data processing procedures are employed to estimate the atmospheric optical turbulence strength from the measured wavefronts.

First, technical background information on optical turbulence, atmospheric turbulence, aero-optical environments, as well as approaches to estimate atmospheric optical turbulence quantities is presented. The experimental campaigns, setups, as well as post-processing procedures are then described. Next, the experimental results are presented and compared with previous experiments as well as literature. Finally, major findings are summarized and future steps are discussed.

III. Background

A. Optical Turbulence

It is useful to begin with the definition of a wavefront. For an electromagnetic wave propagating through space, the wavefront is defined as a locus of points on the surface of the electromagnetic wave with constant phase [3]. In 1678, Christian Huygens postulated that every point on a wavefront could be treated as a source of emitting spherical waves. The envelope of these spherical wavelets at a later instant in time would then describe the new wavefront [3, 4]. Subsequently, light propagates perpendicular to it's wavefront.

The electromagnetic spectrum is comprised of a wide range of wavelengths. For the work presented here, lasers are used which are a single wavelength or narrow wavelength band. As an unperturbed collimated laser is projected through a turbulent environment, the beam is subjected to density fluctuations which consequently, leads to index of refraction fluctuations as defined by the Gladstone-Dale Relation seen in Eq. 1, where n is the index of refraction, K_{GD}, is the

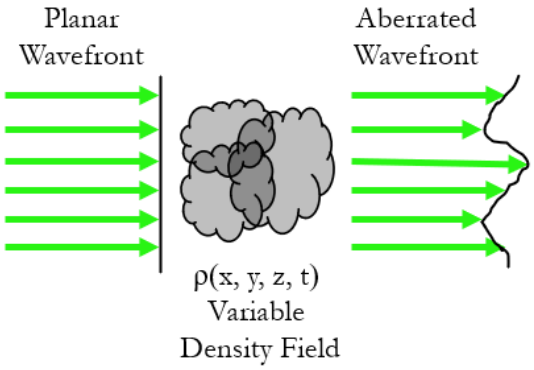

Fig. 1 Beam propagating through inhomogeneous density field.

Gladstone-Dale constant as a function of the laser wavelength, λ, and ρ is the density. In the visible range, K_{GD} can be approximated as $2.27 \times 10^{-4}\ m^3/kg$.

$$n(x, y, z, t) = 1 + K_{GD}(\lambda)\rho(x, y, z, t) \tag{1}$$

These index of refraction fluctuations will aberrate the initially undisturbed beam and cause it to deviate from planarity. An incoming planar wavefront subjected to an inhomogeneous density field is illustrated in Fig. 1.

B. Atmospheric Optical Turbulence

Turbulence is in a continuous state of instability. For a given set of initial conditions, the fluid moves in a trajectory of evolution that is extremely unpredictable [5]. The chaotic nature of turbulent flows makes solving exact equations to predict their behavior virtually intractable. Therefore, simpler models have been developed by studying the behaviors common to turbulent flow-fields.

In 1941, Andrei Kolmogorov presented his theory of turbulence. By employing the assumptions that turbulence is locally homogeneous, locally isotropic, and incompressible, he was able to use a simple dimensional analysis to predict many relevant features of atmospheric turbulence [6]. One observation ubiquitous to turbulent flows is that there must be a source of energy injection. This source of energy occurs at the largest scale structures in the flow. The large-scale structures transport most of their energy to smaller scales through their inertial energy. This transport will continue until it no longer is favorable for inertial forces to be the means of energy transport. More succinctly, the inertial and viscous forces are balanced and the remaining energy is dissipated as heat by means of viscosity. Kolmogorov suggested that in order to make dimensional predictions at the mid-range scales, we should assume that all energy injection occurs at the large scales and energy dissipation occurs at the small scales [6, 7]. In between, there is a constant energy flux. This notion of energy starting at the large scales and decaying to the small scales is referred to as the "energy cascade" and the mid-range of scales which transport the energy is referred to as the "inertial subrange."

1. Index of Refraction Structure Constant

Much of the atmospherics community today still refers to the text of Tatarskii as he applied his predecessor's theoretical constructs to wave propagation in turbulence [8]. Using the ideal gas law ($p = \rho R\mathcal{T}$), and approximating λ as within the visible range of light, a relationship between P, $\mathcal{T}$, ρ, and n exists and is presented in Eq. 2. For changes in the refractive index, dn, it is easy to show that Eq. 2 becomes Eq. 3. For a given altitude, pressure remains fairly constant and temperature fluctuations drive changes in index of refraction. Therefore, this allows Eq. 3 to be further simplified to Eq. 4 [8, 9]. The temperature structure constant, $C^2_{\mathcal{T}}$, is then related to the index of refraction structure constant, C^2_n, through Eq. 5. For laser propagation through the atmosphere, C^2_n is commonly used to quantify optical turbulence strength. This parameter will be referred to heavily throughout this work.

$$n = 1 + 7.77 \cdot 10^{-7} \frac{P}{\mathcal{T}} \tag{2}$$

$$dn = 7.77 \cdot 10^{-7} \frac{P}{\mathcal{T}} \left(\frac{dP}{P} - \frac{d\mathcal{T}}{\mathcal{T}} \right) \tag{3}$$

$$dn = 7.77 \cdot 10^{-7} \frac{P}{\mathcal{T}^2} d\mathcal{T} \tag{4}$$

$$C_n^2 = \left(7.77 \cdot 10^{-7} \frac{P}{\mathcal{T}^2} \right)^2 C_{\mathcal{T}}^2 \tag{5}$$

2. Atmospheric Coherence Length

In addition to C_n^2, the atmospheric coherence length, r_0, is another parameter often used to described optical turbulence environments. The atmospheric coherence length or Fried parameter is heavily used since it elegantly describes the largest size aperture that can be used before atmospheric effects induce appreciable distortions [10]. For apertures larger than r_0, no appreciable improvement in signal to noise is achieved. A larger aperture gathers more light which increases the amount of signal collected, but it also allows for greater phase variation across the aperture in an environment of Kolmogorov turbulence [11]. For environments of constant C_n^2 (horizontal propagation paths), the relationship between r_0 and C_n^2 is described by Eq. 6 for spherical waves [12, 13]. Here, Z is the propagation distance and k is the wavenumber described as $2\pi/\lambda$ where λ is the laser wavelength.

$$r_0 = 3.0\left(C_n^2 Z k^2\right)^{-3/5} \tag{6}$$

3. Optical Turbulence Models

It is well known that there are higher levels of turbulence close to Earth's surface and lower values at higher altitudes. With higher altitudes, the temperature decreases corresponding to a less dense atmosphere, resulting in lower turbulence levels. One of the most popular atmospheric optical turbulence models is known as the Hufnagel-Valley Boundary model (HVB) as seen in Eq. 7, where z is the altitude above ground level.

$$C_n^2(z) = 5.94{\times}10^{-23} z^{10} e^{-z} \left(\frac{U_c}{27} \right)^2 + 2.7{\times}10^{-16} e^{-2z/3} + A e^{-10z} \tag{7}$$

HVB only uses two input parameters, U_c and A. The variable U_c is the approximate high-altitude wind speed and A is an input to account for near ground conditions. When U_c and A are taken to be 21 m/s and 1.7×10^{-14} $m^{-2/3}$, respectively, this corresponds to an atmospheric coherence length of $r_0 = 5$ $[cm]$ and an isoplanatic angle, which is another commonly used atmospheric optical turbulence parameter, of $\theta_0 = 7$ μrad [12]. Fittingly, this specialized form of the model is referred to as HV57.

Two other turbulence models commonly referenced are the Clear 1 night model as well as the Submarine Laser Communication (SLC) night model [12]. These two models along with HV57 are plotted versus altitude in Fig. 2. Later on, C_n^2 values are estimated from the experimental data for varying altitudes and the results are compared with these turbulence profiles.

Measuring C_n^2 over a path length is typically referred to as "turbulence profiling [14]." Previous experimental flight campaigns were conducted using AAOL which sought to measure optical turbulence strength on a slant path from a stationary ground station to an orbiting air station. These experimental campaigns are not the emphasis of the work presented here. However, some results from these campaigns are presented for comparison purposes. These results are shown in Fig. 3. Each plot presents experimentally measured C_n^2 values as a function of altitude for different aircraft orbits. The green dotted line also plotted is the HV57 model for reference. The C_n^2 values estimated from the experimental work presented here are also compared with these previous experimental results. For much greater detail on these test campaigns, see Refs. [15–17].

C. Aero-Optical Environments

For the experimental work in this manuscript, distortions are imposed onto the laser beam from both the atmosphere as well as the aero-optical environment in proximity of the aircraft. Therefore, despite atmospheric optical turbulence being the emphasis of the work, it is also important to understand how aero-optical environments affect the laser beam. First, the background of the field of aero-optics is discussed. Then, equations to quantify and scale aero-optical distortions are presented.

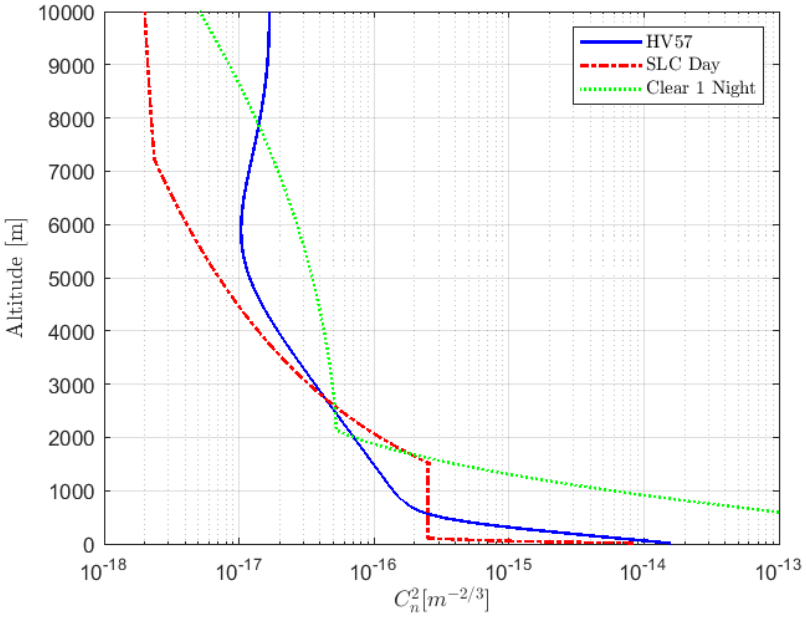

Fig. 2 Various turbulence profile models plotted versus altitude.

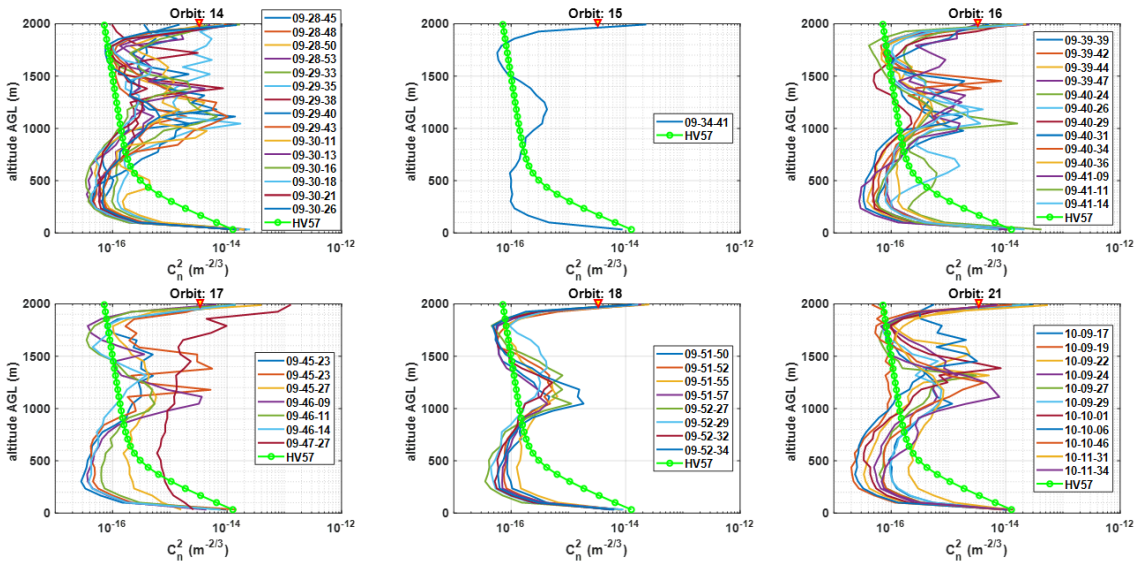

Fig. 3 Experimentally measured turbulence profiles [15–17].

1. Background

Interest in developing airborne high-energy laser (HEL) weapon systems since the Airborne Laser Laboratory (ALL) in the late 1970's and early 1980's [18]. The ALL program used a CO_2 laser, which lased at 10.6 μm. The ALL program was successful however it was believed that in order to increase the capability of airborne HEL systems, a shorter wavelength laser needed to be used. As described in Refs. [19–21], the shorter the laser wavelength, the higher the intensity on-target given the same system laser exit pupil diameter and power in the absence of aberrating effects [22]. As such, interest and research have gravitated towards the use of near visible wavelength HELs. Since the days of ALL, HELs have achieved the goal of decreasing laser wavelength. The Airborne Laser (ABL) used a Chemical Oxygen-Iodine Laser (COIL) which lased at 1.315 μm. The latest development of solid-state lasers use an even shorter wavelength of 1.064 μm. Unfortunately, the effect of aberrations imposed onto lasers beams of shorter wavelengths result in greater energy spread in the far-field compared to longer wavelength lasers [19–21]. When shorter wavelength lasers are used, the optical turbulence associated with the aerodynamics in proximity to the beam director was identified as an important research problem. Hence, extensive research into the field, which we today refer to as Aero-Optics was inspired and conducted.

2. Quantification

The Optical Path Length (OPL) and Optical Path Difference (OPD) are typically used to quantity the severity of the aberrations imposed onto a laser through an aero-optical environment. The OPL is defined as the path integral of the index of refraction as defined by Eq. 8, where z is the propagation direction [20].

$$OPL(x, y, t) = \int_{z_1}^{z_2} n(x, y, z, t) dz \tag{8}$$

The OPD is the result of removing the spatial mean (or piston) from the OPL as shown in Eq. 9.

$$OPD(x, y, t) = OPL(x, y, t) - \overline{OPL(x, y, t)} \tag{9}$$

OPD is often simplified as the conjugate of the wavefront, $OPD(x, y, t) = -W(x, y, t)$. By taking the root mean square of the $OPD(x, y, t)$ in space, we get the $OPD_{RMS}(t)$ which describes the wavefront's time-dependent departure from planarity, as described in Eq. 10 where the brackets indicate spatial averaging [21].

$$OPD_{RMS}(t) = \sqrt{\overline{OPD(x, y, t)^2}} \tag{10}$$

Furthermore, time averaging yields the OPD_{RMS} which is the most common metric for diagnosing the severity of beam aberrations through aero-optical environments.

3. Boundary Layer Scaling

In recent years, aero-optical boundary layers have been heavily researched. Many of the major findings are summarized in Ref. [23]. Important scaling laws have been developed which allow the optical distortions associated with canonical boundary layers to be scaled to different freestream conditions. For subsonic, turbulent boundary layers, OPD_{RMS} scales as

$$OPD_{RMS} \approx 0.19 K_{GD} \rho_\infty M^2 \delta_{BL} \sqrt{C_f} G(M). \tag{11}$$

Here, ρ_∞ is the freestream density, M is the cruise Mach number, δ_{BL} is the boundary layer thickness, C_f is the skin friction coefficient, and $G(M)$ is a function which can be approximated as $G(M) \approx 1 - 0.19M^2 + 0.03M^4$. For greater detail on the development, assumptions, and limitations of Eq. 11, see Ref. [23]. Equation 11 is used later in this work to scale empirical AAOL boundary layer data to freestream conditions at different altitudes. The scaled OPD_{RMS} associated with the turbulent boundary layer of the aircraft is then used to estimate the aero-optical contribution to aberrations on a beam which propagated through both the atmosphere as well as the aero-optical environment.

D. Estimating Optical Turbulence Parameters

Now that both atmospheric optical turbulence as well as aero-optical environments have been introduced, the following section describes two approaches for estimating optical turbulence parameters from the measured wavefronts.

1. Phase Variance

The atmospheric coherence length, r_0, is related to the variances of optical phase quantities [24]. A common approach to estimate r_0 from wavefront measurements is to use the tilt-removed phase variance, $\sigma^2_{\phi_{HO}}$, described in Eq. 12 [25]. In this equation, subscript 'HO' is used to indicated "higher-order" and D is the aperture diameter. If r_0 is known, Eq. 6 can then be used to approximate C_n^2 assuming horizontal propagation paths.

$$\sigma^2_{\phi_{HO}} = 0.134\left(\frac{D}{r_0}\right)^{5/3} \tag{12}$$

The estimate of r_0 using phase variance will be affected if phase distortions from the turbulent boundary layer and acoustic environment are present. However, if the phase variances associated with the aero-optical, $\sigma^2_{\phi_{AO}}$, and acoustical distortions, $\sigma^2_{\phi_{Acoustic}}$, are known, the phase variance from the atmospheric induced aberrations can be estimated using Eq. 13. In this equation, $\sigma^2_{\phi ALL}$ is the overall phase variance. OPD_{RMS} is related to optical phase by $\sigma^2_{\phi_{AO}} = \left(\frac{2\pi OPD_{RMS}}{\lambda}\right)^2$. Therefore, Eq. 11 can be used to approximate $\sigma^2_{\phi_{AO}}$ of the boundary layer for data collected at any altitude.

A detailed procedure for estimating the OPD_{RMS} associated with the acoustic environments is described in Ref. [26]. For the purposes of the work presented here, it is assumed that the OPD_{RMS} associated with the acoustical distortions remains fairly constant with altitude. This is not exactly true however this approximation does not drastically influence results.

Once $\sigma^2_{\phi_{AO}}$ and $\sigma^2_{\phi_{Acoustic}}$, $\sigma^2_{\phi_{ATM}}$ can be approximated using Eq. 13. $\sigma^2_{\phi_{ATM}}$ can then be used in Eq. 12 to estimate r_0.

$$\sigma^2_{\phi_{ATM}} = \sigma^2_{\phi ALL} - \sigma^2_{\phi_{AO}} - \sigma^2_{\phi_{Acoustic}} \tag{13}$$

2. Slope Discrepancy

In recent years, a quantity referred to as "slope discrepancy" has been used to estimate optical turbulence parameters with high fidelity. Slope discrepancy is only briefly described here but much more information on this quantity can be found in Refs. [24, 27, 28]. Slope discrepancy is a result of using a least squares reconstructor to convert measured slopes from a SHWFS into reconstructed phase. Slope discrepancy, symbolized by δ, is the component of phase which is not accounted for when using a least squares reconstructor - mathematically referred to as the curl of the vector potential [27]. In other words, slope discrepancy is the difference between the slopes measured by a SHWFS and the gradient of the reconstructed phase. In order to use slope discrepancy as a means for extracting turbulence parameters, a slope discrepancy structure function is calculated. The equation for this structure function, E^2_{SD}, is presented in Eq. 14 [24].

$$E^2_{SD}(\tau) = \left\langle |\delta(t+\tau) - \delta(t)|^2 \right\rangle \tag{14}$$

Slope discrepancy results from subaperture fitting error, η, measurement noise, μ, and discontinuities such as branch points or shock waves. In this work, we assume that branch points and shock waves are nonexistent. This assumption is valid since experimental data was not collected in what is regarded as "deep turbulence." In other words, the Rytov parameter is sufficiently small (below 0.3). Additionally, since there were no geometries protruding into the freestream flow in front of the acquisition aperture, no shock waves were present. Therefore, slope discrepancy can be described as, $\delta = \eta + \mu$. Plugging this into Eq. 14, expanding, and simplifying negligible components leads to the following result,

$$E^2_{SD}(\tau) = E^2_{\eta}(\tau) + 2\sigma^2_{\mu}. \tag{15}$$

The slope discrepancy structure function, $E^2_{SD}(\tau)$, is equal to the fitting error structure function, $E^2_{\eta}(\tau)$, plus two times the noise variance, σ^2_{μ}. The assumptions imposed to get Eq. 15 are discussed in Ref. [24]. The asymptotes of the slope discrepancy structure function lead to an important result. The fitting error variance, σ^2_{η}, can be described as follows,

$$\sigma^2_{\eta} = \frac{1}{2}\left(E^2_{SD}(T) - E^2_{SD}(0)\right). \tag{16}$$

Table 1 Data points collected during flight 1 and 2 [2].

Approximate Altitude [m]	Approximate Separation [m]					
	750	1500	2300	3000	3300	3700
762		X				
914		X				
1219		X				
1372	X	X				
1524	XO	XO	X	X	X	X
1829	X	X	XO	X	X	X
2134			O			
3048	O	O	O	O		

O: Flight 1; X: Flight 2; Shaded Blue: Data collected over water

The term $E_{SD}^2(0)$, or the asymptote for short time delays, represents twice the noise variance and the asymptote at large time delays, $E_{SD}^2(T)$, represents twice the fitting error variance, σ_η^2. The fitting error variance is then related to r_0 by Eq. 17.

$$\sigma_\eta^2 = \alpha\left(\frac{d}{r_0}\right)^{5/3} \tag{17}$$

Here, α is a constant specific to the geometry of the SHWFS used and d is the subaperture width. The α constant can be found analytically [29], however, finding alpha computationally yields a better estimate.

Equation 15 elegantly describes that the overall slope discrepancy is a combination of fitting error from the atmosphere as well as measurement noise. However, how would this equation change if distortions from the aero-optical and aero-acoustical environments were also present? Recent work has demonstrated that if fitting error from the aero-optical/aero-acoustical environment is also present in the data and uncorrelated with fitting error from the atmosphere, Eq. 18 can be rewritten as follows,

$$E_{SD}^2(\tau) = E_\eta^2(\tau) + E_\gamma^2(\tau) + 2\sigma_\mu^2. \tag{18}$$

Here, γ is the slope discrepancy from the aero-optical/aero-acoustical environments and $E_\gamma^2(\tau)$ is the associated fitting error structure function. This is an important result. If we know $E_\gamma^2(\tau)$, we can estimate $E_\eta^2(\tau)$ by simply measuring the total slope discrepancy structure function, $E_{SD}^2(\tau)$.

This slope discrepancy approach along with the phase variance approach described in the section above are used to approximate r_0 and C_n^2 from data collected in the experimental campaigns described in the next section.

IV. Experimental Campaigns and Data Processing

A. Campaign Objectives

As discussed above, wavefronts are collected at both varying altitudes and separations. The details pertaining to the data points collected in the two flights are presented in Table 1. Flight 1 was conducted in the afternoon on 07 March 2020 and flight 2 was conducted in the late morning to early afternoon on 17 March 2020. Both flights were conducted over the Northern Michigan area. Wavefronts were collected at both 4 and 10 kHz with an exposure time of both 0.4 and 1 μs. The aircraft consistently flew at a cruise Mach number of 0.4. A total of 28,000 frames were collected per data point [2].

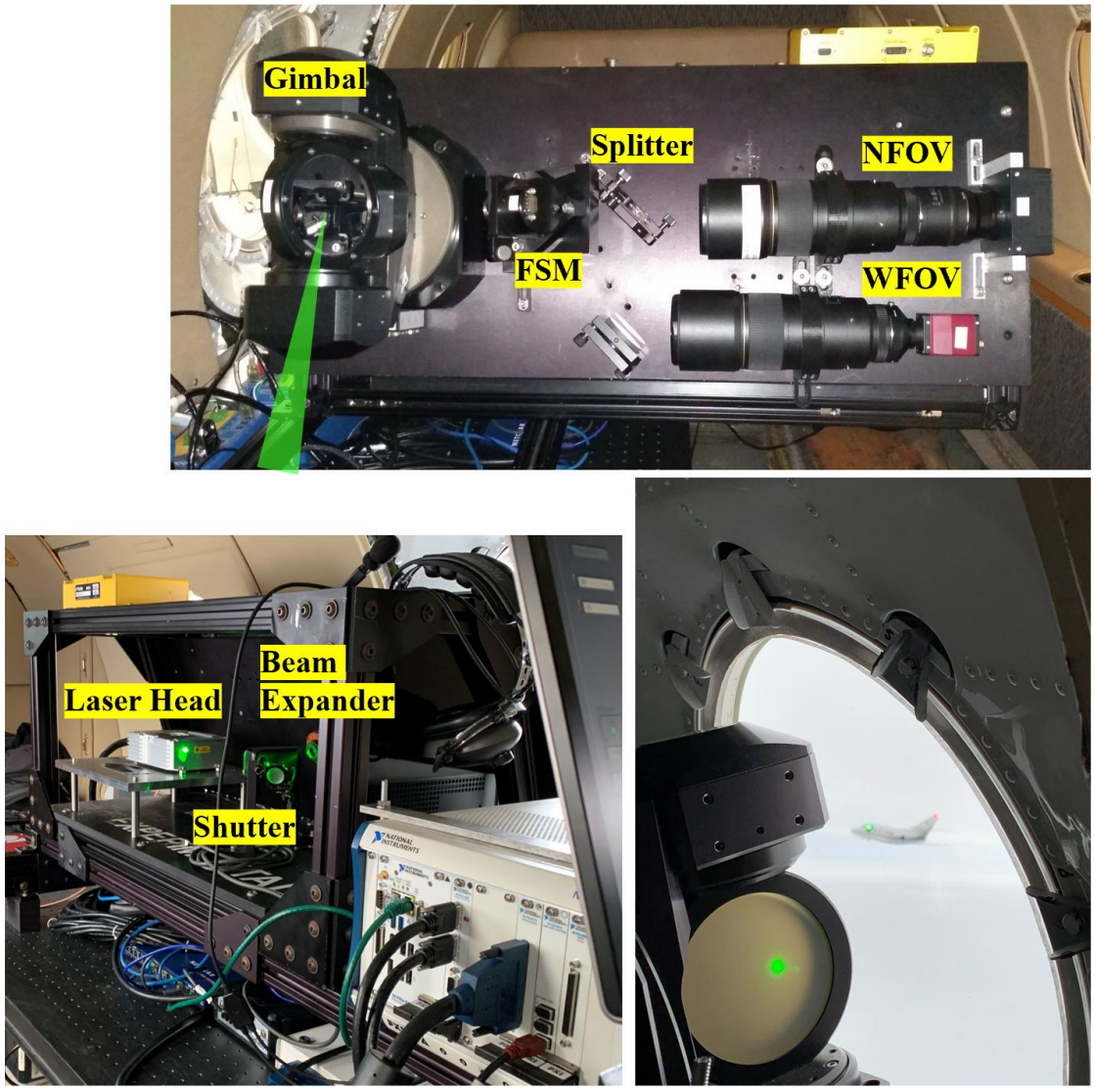

Fig. 4 AAOL source aircraft setup.

B. Source Aircraft

The source aircraft is equipped with a Laser Quantum Opus 532 nm 0-2 variable watt laser, motorized system to vary beam divergence, a 50 mm diameter OIM102 fast steering mirror (FSM), an AeroTech gimbal with a 100 mm mirror, a National Instruments PXI Real-Time system, a laptop for user control, and a GPS unit which allows relative aircraft displacements to be calculated. This system allows for both image and return based tracking capability. Figure 4 illustrates the experimental setup in the source aircraft. A wide field of view (WFOV) camera with a 300 mm lens was used to locate the laboratory aircraft and the narrow field of view (NFOV) camera with a 600 mm lens was used for tracking – either off the return signal or image features of the other aircraft. Using the motorized beam divergence system, the divergence of the outgoing beam can be changed by the user to sufficiently fill the acquisition window on the laboratory aircraft window regardless of the separation distance between aircraft [2].

C. Laboratory Aircraft

The laboratory aircraft receives the incoming beam from the source aircraft and directs the beam to a Shack Hartmann Wavefront Sensor (SHWFS) installed on a high-speed camera. Figure 5 illustrates the experimental setup of this aircraft. Here, the beam enters through the optical quality window then is directed off a 304.8 mm flat steering

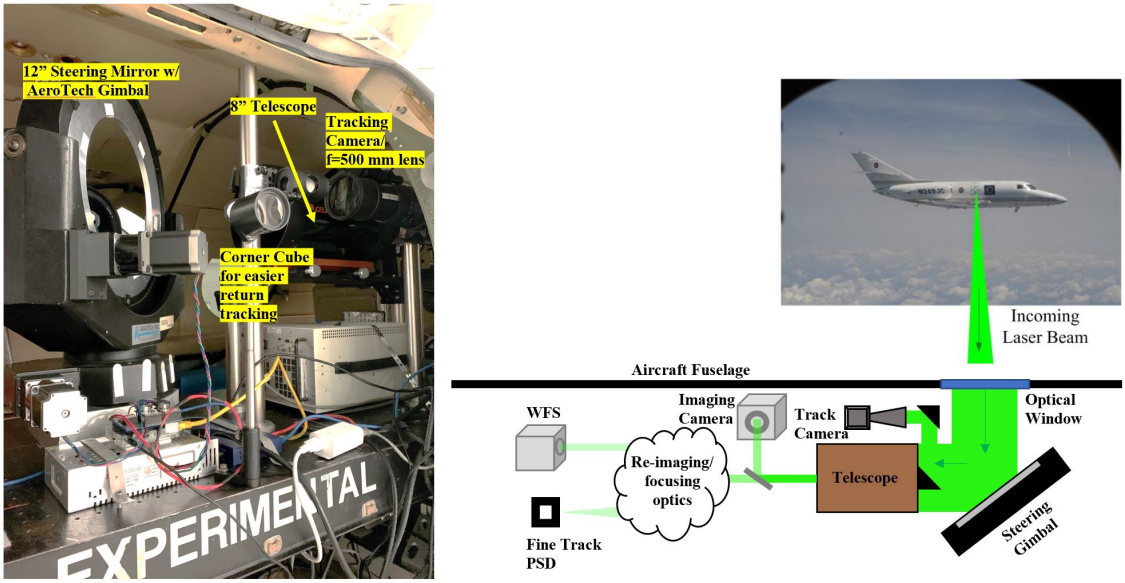

Fig. 5 AAOL laboratory aircraft setup.

mirror mounted on an AeroTech gimbal. To stabilize the incoming beam, a computer-controlled proportional feedback system was employed. The gimbal forwards the beam through a Schmidt-Cassegrain telescope with a diameter of 203 mm and a central obscuration of 64 mm in diameter. A mirror is mounted on the back of the telescope's secondary mirror in order to pick off a portion of the beam for the tracking camera which has a 500 mm focal length lens attached. After exiting the telescope, a portion of the beam is directed to an imaging camera and the other portion of the beam is split again to be partitioned between an On-Trak PSM2-10 position sensing device (PSD) as well as the SHWFS. The PSD sends velocity commands to the gimbal and serves as the fine track system. The SHWFS has a spatial resolution of 50×50 subapertures 0.3 mm in size, allowing the wavefront distortions imposed on the beam to be measured with great spatial resolution. Wavefronts were acquired at both 4 and 10 kHz. A corner cube was also installed at the bottom of the aircraft acquisition window, ensuring that the source aircraft received a strong return signal for tracking at large separations.

D. Processing Procedure

In order to convert the measured slopes into usable wavefront measurements, various data processing steps need to be employed. Firstly, the measured slopes are converted into phase using a least squares reconstructor. Next, since mechanical contamination manifests as tip/tilt that is coupled with the turbulence induced component, all tip/tilt and the mean component (or piston) are initially removed from the data. Lastly, in experimental processing, steady lensing is also removed from the data. Steady lensing are distortions that manifest in the data which remain constant with time. Lensing can result from scratches or dirty optics, or slow moving temperature gradients in the lab. After these initial data processing steps have been done, post processing-procedures to estimate atmospheric optical turbulence parameters can be employed.

V. Results and Discussion

A. Close Propagation Distances

In order to estimate the wavefront error imposed by the aero-optical and aero-acoustical environments in flight, wavefront measurements were collected at close aircraft separations (≈ 50 m) and higher altitudes ($\approx 3,000$ m) using AAOL. By doing so, the presumption is that negligible atmospheric distortions are imposed onto the beam. The same experimental setup described in Section IV.A was used and the processing procedure described in Section IV.D was applied to the measured wavefronts.

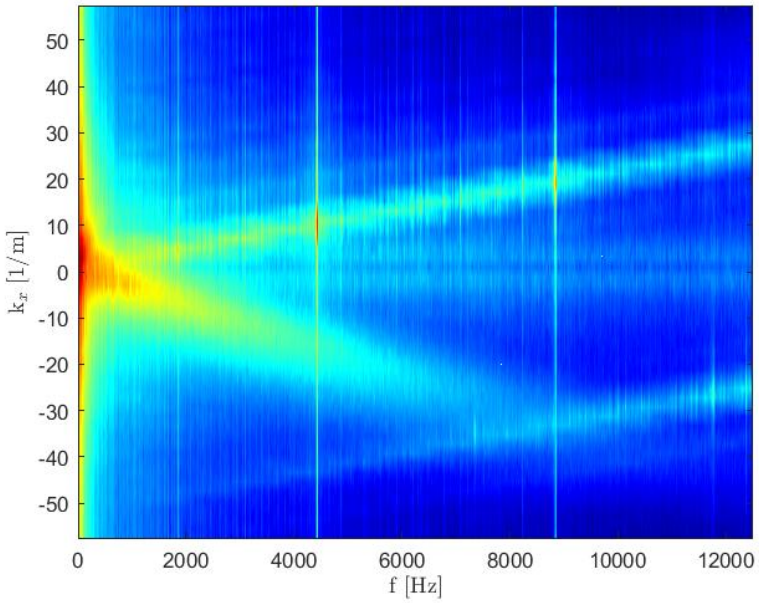

Fig. 6 Dispersion analysis for wavefront data collected at close aircraft separations and high altitude.

Previous studies have been successful at decoupling acoustic and aero-optical related disturbances using a three-dimensional fast Fourier transform, otherwise known as a dispersion analysis. Since the acoustic structures seen in the flight data are upstream propagating (opposite the direction of convective turbulent structures), the dispersion analysis can also be used here to isolate and remove this source of wavefront aberrations [1, 26]. Here, the spatial and temporal domains are transformed into the wavenumber and frequency domains. The forward transform is described in Eq. 19.

$$\widehat{OPD}(f_t, k_x, k_y) = \int_{-\infty}^{\infty}\int_{-\infty}^{\infty}\int_{-\infty}^{\infty} OPD(t,x,y)e^{-i(2\pi f_t t - k_x x - k_y y)}dtdxdy \tag{19}$$

In the spectral domain, the positive wavenumber-positive temporal frequency as well as the negative wavenumber-negative temporal frequency domains correspond to the upstream traveling acoustic component, assuming flow is going from left to right. Conversely, the negative wavenumber-positive temporal frequency as well as the positive wavenumber-negative temporal frequency domains correspond to the downstream traveling turbulent convective structures. Separating these components into their respective spectral quadrants and inverse transforming allows the upstream and downstream structures to be decoupled into their respective spatial-temporal data sets. For greater detail on using dispersion analysis to decouple aero-optical and acoustic optical turbulence distortions, see Refs. [1, 26].

Dispersion analysis was used here in order to decouple the distortions from the turbulent boundary layer and the distortions from the upstream propagating acoustic waves. Figure 6 presents the resultant dispersion analysis. The strong peak at a temporal frequency of approximately 4, 500 Hz represents the blade pass frequency of the jet engine. After separating the dispersion analysis into upstream and downstream propagating components and inverse Fourier transforming, it was found that the OPD_{RMS} associated with the boundary layer was approximately 1.98×10^{-8} m and the OPD_{RMS} of the acoustic contamination was approximately 2.57×10^{-8} m.

As mentioned above, in this work, we will assume that the acoustic contamination remains fairly constant with altitude. However, in order to see how the OPD_{RMS} associated with the turbulent boundary layer scales with altitude, we use Eq. 11. The result of this for varying altitudes can be seen in Fig. 7. Here, the yellow star indicates the altitude where the empirical data was collected.

B. Estimating Atmospheric Optical Turbulence Parameters

Using the approaches discussed in Section III.D, C_n^2 is estimated from the wavefront measurements collected at both varying altitudes as well as aircraft separations. Figure 8 presents the C_n^2 values estimated from the wavefront

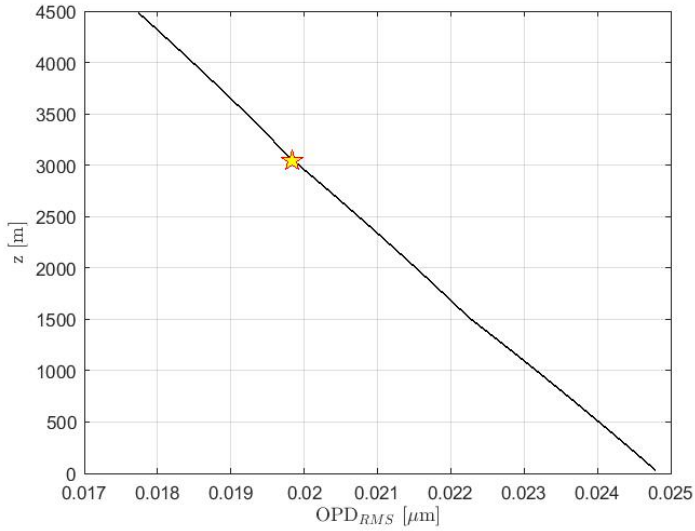

Fig. 7 OPD_{RMS} **altitude scaling for a subsonic turbulent boundary layer.**

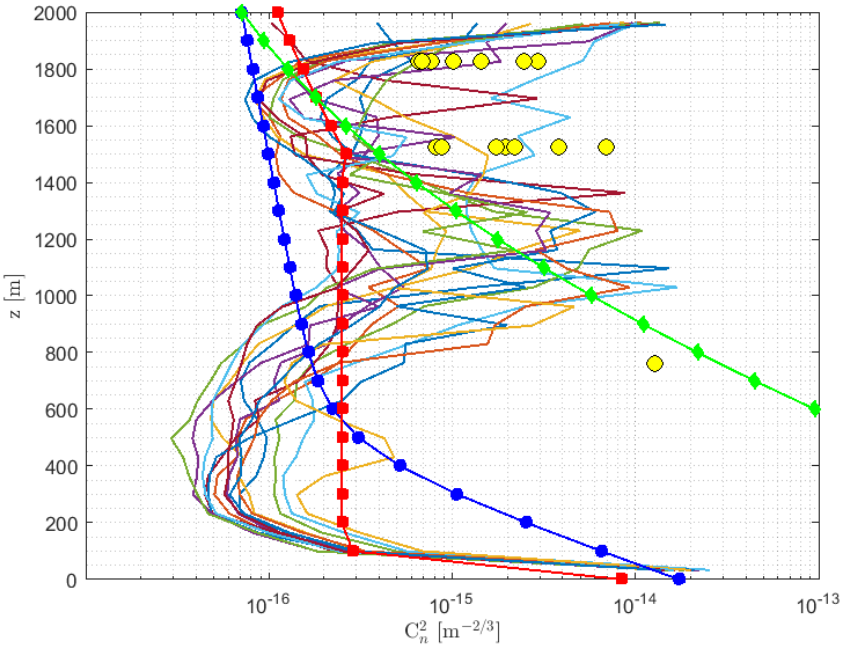

Fig. 8 C_n^2 **values estimated using the phase variance approach.**

measurements using the phase variance approach. These results are plotted as yellow circles. The estimated acoustic and aero-optical distortions were removed using Eq. 13 coupled with the results from Section V.A. Also plotted on Fig. 8 are the three turbulence models discussed in Section III.B.3. The HV57 model is represented by a blue line with circle markers, the SLC Night model is represented by a red line with square markers, and the Clear 1 Night model is represented by a green line and diamond markers. The results from the previous experimental turbulence profiling campaign also discussed in Section III.B.3 are plotted as solid lines without markers. Each solid line represents a different data collection. It can be see that C_n^2 values estimated using the phase variance approach are larger than the C_n^2 values predicted by the turbulence models. However, the measured C_n^2 values have some agreement with the results

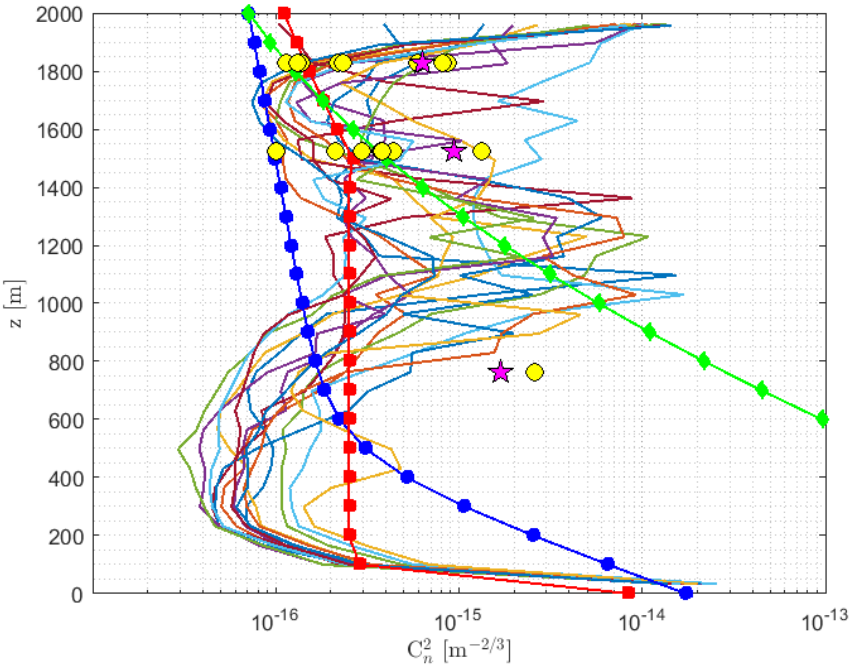

Fig. 9 C_n^2 values estimated using the slope discrepancy approach.

from the previous turbulence profiling campaigns. The C_n^2 results estimated using the slope discrepancy are plotted in Fig. 9. Again, the turbulence models and results from the previous turbulence profiling campaign are also presented. The C_n^2 estimates calculated using slope discrepancy are represented by yellow circles. These estimates did not take into account aero-optical and aero-acoustical contamination. The data collected during the campaigns discussed in this document were collected at relatively slow sample rates. In order to more effectively remove aero-optical and aero-acoustical contamination from the slope discrepancy structure function by using Eq. 18, the time between samples needs to be short. However, for three data points, aero-optical and aero-acoustical contamination was able to be removed using the slope discrepancy approach described in Eq. 18. These results are indicated on the plot with pink star markers. It can be seen that when aero-optical and aero-acoustical contamination is removed, the C_n^2 estimate decreases. This is expected since the aero-optical environment does have some fitting error. In general, the C_n^2 results obtained using the slope discrepancy approach show better agreement with both the turbulence models as well as the previous experimental measurements compared to the phase variance approach. The agreement between C_n^2 estimates and the turbulence models as well as the experimental results from the previous turbulence profiling campaign is particularly good at altitudes between 1400 and 1800 m.

VI. Conclusions

Experimental campaigns were conducted which sought to measure distortions imposed onto a laser beam by the atmosphere. The distortions imposed onto the laser beam would then be used to quantify the optical atmospheric turbulence strength of the atmosphere through which the laser beam propagated. Wavefront measurements were collected at both varying altitudes as well as aircraft separations. The measured phase variance as well as slope discrepancy were used to estimate r_0 and subsequently, C_n^2. The aero-optical, aero-acoustical, and mechanical environments in and around the aircraft introduce contamination into the estimates of C_n^2. This work also describes how to account for these sources of error.

The C_n^2 estimates were compared with optical turbulence models as well as experimental results from a previous test campaign. The C_n^2 estimates calculated from the phase variance were generally higher than what models predict. The C_n^2 estimates calculated using the slope discrepancy approach were in agreement with both the atmospheric optical turbulence models as well as the results from the previous experimental turbulence profiling campaigns.

Acknowledgments

This work is supported by the Joint Technology Office, Grant number FA9550-13-1-0001 and Office of Naval Research, Grant number N00014-18-1-2112. The U.S. Government is authorized to reproduce and distribute reprints for governmental purposes notwithstanding any copyright notation thereon.

References

[1] Kalensky, M., Gordeyev, S., and Jumper, E. J., "In-Flight Studies of Aero-Optical Distortions Around AAOL-BC," *2019 Aviation Forum*, American Institute of Aeronautics and Astronautics, 2019. https://doi.org/10.2514/6.2019-3253.

[2] Kalensky, M., Jumper, E., Gordeyev, S., Archibald, A., and Kemnetz, M. R., "Experimental Investigation of Atmospheric Induced Beam Jitter," *2021 SciTech Forum*, American Institute of Aeronautics and Astronautics, 2021. https://doi.org/10.2514/6.2021-0334.

[3] Klein, M. V., Furtak, T. E., and Klein, D., *Optics*, John Wiley & Sons, 1986. URL https://www.ebook.de/de/product/4242011/miles_v_klein_thomas_e_furtak_dave_klein_optics.html.

[4] Goodman, J., *Introduction to Fourier optics*, Roberts & Co, Englewood, Colo, 2005.

[5] Tennekes, H., *A first course in turbulence*, The MIT Press, Cambridge, Massachusetts, 1972.

[6] Kolmogorov, A., "Dissipation of energy in the locally isotropic turbulence," *Proceedings of the Royal Society*, Vol. 434, No. 1890, 1991, pp. 15–17. https://doi.org/10.1098/rspa.1991.0076.

[7] Kolmogorov, A., "The local structure of turbulence in incompressible viscous fluid for very large Reynolds numbers," *Proceedings of the Royal Society*, Vol. 434, No. 1890, 1991, pp. 9–13. https://doi.org/10.1098/rspa.1991.0075.

[8] Tatarskii, V., *Wave propagation in a turbulent medium*, Dover Publications, Inc, Mineola, New York, 2016.

[9] Siegenthaler, J., Jumper, E., and Gordeyev, S., "Atmospheric Propagation vs. Aero-Optics," *2008 SciTech Forum*, American Institute of Aeronautics and Astronautics, 2008. https://doi.org/10.2514/6.2008-1076.

[10] Fried, D. L., and Mevers, G. E., "Evaluation of ro for Propagation Down Through the Atmosphere," *Applied Optics*, Vol. 13, No. 11, 1974, p. 2620. https://doi.org/10.1364/ao.13.002620.

[11] Siegenthaler, J. P., "GUIDELINES FOR ADAPTIVE-OPTIC CORRECTION BASED ON APERTUREFILTRATION," Ph.D. thesis, University of Notre Dame, 2008.

[12] Tyson, R., *Principles of adaptive optics*, CRC Press, Boca Raton, FL, 2011.

[13] Fried, D., "Optical heterodyne detection of an atmospherically distorted signal wave front," *IEEE*, Vol. 55, No. 1, 1967, pp. 57–77. https://doi.org/10.1109/proc.1967.5377.

[14] Whiteley, M., "Differential-tilt technique for saturation-resistant profiling of atmospheric turbulence," Tech. rep., MZA Associates Corporation, 2002.

[15] Kalensky, M., Jumper, E., Whiteley, M., Diskin, Y., Gordeyev, S., Drye, R., Archibald, A., and Grose, M., "Turbulence Profiling Using AAOL-BC," *2020 SciTech Forum*, American Institute of Aeronautics and Astronautics, 2020. https://doi.org/10.2514/6.2020-0682.

[16] Diskin, Y., Grose, M., Whiteley, M., Kalensky, M., Jumper, E., Gordeyev, S., and Archibald, A., "Atmospheric and Aero Disturbance Characterization for DE System Applications," *2020 Aviation Forum*, American Institute of Aeronautics and Astronautics, 2020. https://doi.org/10.2514/6.2020-3234.

[17] Diskin, Y., Whiteley, M., Grose, M., Jackovitz, K., Drye, R., Hampshire, B., Owens, M., Smith, E., Magee, E., Kalensky, M., Jumper, E., Gordeyev, S., and Archibald, A., "Aircraft to Ground Profiling: Turbulence Measurements and Optical System Performance Modeling," *AIAA Journal*, Vol. 59, No. 11, 2021, pp. 4610–4625. https://doi.org/10.2514/1.j060580.

[18] Duffner, R., *Airborne laser : bullets of light*, Plenum Trade, New York, 1997.

[19] Gilbert, K., *Aero-optical phenomena*, American Institute of Aeronautics and Astronautics, New York, N.Y, 1982.

[20] Jumper, E. J., and Fitzgerald, E. J., "Recent advances in aero-optics," *Progress in Aerospace Sciences*, Vol. 37, No. 3, 2001, pp. 299–339. https://doi.org/10.1016/s0376-0421(01)00008-2.

[21] Jumper, E. J., and Gordeyev, S., "Physics and Measurement of Aero-Optical Effects: Past and Present," *Annual Review of Fluid Mechanics*, Vol. 49, No. 1, 2017, pp. 419–441. https://doi.org/10.1146/annurev-fluid-010816-060315.

[22] Kyrazis, D. T., "Airborne Laser Laboratory departure from Kirtland Air Force Base and a brief history of aero-optics," *Optical Engineering*, Vol. 52, No. 7, 2012, p. 071403. https://doi.org/10.1117/1.oe.52.7.071403.

[23] Gordeyev, S., Smith, A. E., Cress, J. A., and Jumper, E. J., "Experimental studies of aero-optical properties of subsonic turbulent boundary layers," *Journal of Fluid Mechanics*, Vol. 740, 2014, pp. 214–253. https://doi.org/10.1017/jfm.2013.658.

[24] Brennan, T. J., and Mann, D. C., "Estimation of optical turbulence characteristics from Shack Hartmann wavefront sensor measurements," *Proceedings of SPIE*, edited by D. C. Dayton, T. A. Rhoadarmer, and D. J. Sanchez, SPIE, 2010. https://doi.org/10.1117/12.862808.

[25] Noll, R. J., "Zernike polynomials and atmospheric turbulence," *Journal of the Optical Society of America*, Vol. 66, No. 3, 1976, p. 207. https://doi.org/10.1364/josa.66.000207.

[26] Gordeyev, S., and Kalensky, M., "Effects of Engine Acoustic Waves on Aerooptical Environment in Subsonic Flight," *AIAA Journal*, Vol. 58, No. 12, 2020, pp. 5306–5317. https://doi.org/10.2514/1.j059484.

[27] Tyler, G. A., "Reconstruction and assessment of the least-squares and slope discrepancy components of the phase," *Journal of the Optical Society of America*, Vol. 17, No. 10, 2000, p. 1828. https://doi.org/10.1364/josaa.17.001828.

[28] Winker, D. M., Ameer, G. A., Brown, S. L., Cochran, G. C., Dueck, R., Fried, D. L., Lussier, D. M., Moretti, W., Roberts, P. H., Steinhoff, K. E., and Tyler, G. A., "Characteristics Of Turbulence Measured On A Large Aperture," *Proceedings of SPIE*, edited by N. S. Kopeika and W. B. Miller, SPIE, 1988. https://doi.org/10.1117/12.945810.

[29] Vaughn, J., "The Variability of r0 Estimates," Tech. rep., The Optical Sciences Company, 2002.